JOURNAL OF SYNCHROTRON RADIATION

ISSN 1600-5775

Received 20 August 2020
Accepted 16 December 2020

Edited by P. A. Pianetta, SLAC National Accelerator Laboratory, USA

Keywords: GaP/Ge; high-resolution X-ray diffraction; X-ray absorption fine structure.

Effect of germanium auto-diffusion on the bond lengths of Ga and P atoms in GaP/Ge(111) investigated by using X-ray absorption spectroscopy

R. Roychowdhury,[a,b]* P. Rajput,[c] Shailendra Kumar,[d]* R. Kumar,[a,b] A. Bose,[a,b] S. N. Jha,[a,c] T. K. Sharma[a,b] and V. K. Dixit[a,b]*

[a]Training School Complex, Homi Bhabha National Institute, Anushakti Nagar, Mumbai, India, [b]Raja Ramanna Centre for Advanced Technology, Indore, Madhya Pradesh 452013, India, [c]Atomic and Molecular Physics Division, Bhabha Atomic Research Centre, Trombay, Mumbai 400085, India, and [d]UGC-DAE Consortium for Scientific Research, Indore, Madhya Pradesh, India. *Correspondence e-mail: rijul@rrcat.gov.in, agnisk.kumar58@gmail.com, dixit@rrcat.gov.in

The germanium auto-diffusion effects on the inter-atomic distance between the nearest neighbors of the Ga atom in GaP epilayers are investigated using high-resolution X-ray diffraction (HRXRD) and X-ray absorption spectroscopy. The GaP layers grown on Ge (111) are structurally coherent and relaxed but they show the presence of residual strain which is attributed to the auto-diffusion of Ge from the results of secondary ion mass spectrometry and electrochemical capacitance voltage measurements. Subsequently, the inter-atomic distances between the nearest neighbors of Ga atom in GaP are determined from X-ray absorption fine-structure spectra performed at the Ga *K*-edge. The estimated local bond lengths of Ga with its first and second nearest neighbors show asymmetric variation for the in-plane and out-of-plane direction of GaP/Ge(111). The magnitude and direction of in-plane and out-of-plane microscopic residual strain present in the GaP/Ge are calculated from the difference in bond lengths which explains the presence of macroscopic residual tensile strain estimated from HRXRD. Modified nearest neighbor configurations of Ga in the auto-diffused GaP epilayer are proposed for new possibilities within the GaP/Ge hetero-structure, such as the conversion from indirect to direct band structures and engineering the tensile strain quantum dot structures on (111) surfaces.

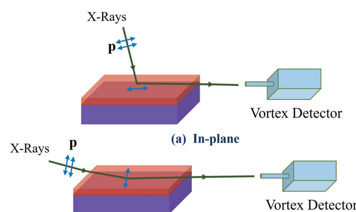

© 2021 International Union of Crystallography

1. Introduction

High crystalline III–V semiconductor epitaxial layer growth on Si and Ge substrates is the prime requirement for the implementation of efficient and economically viable nano-photonic devices. In the recent past, enormous efforts have been made for the integration of GaP and GaAs epilayers and their nanostructures on Si and Ge substrates (Liebich *et al.*, 2011; Chen *et al.*, 2016; Grassman *et al.*, 2013; Kumar *et al.*, 2016*a*; Supplie, May, Steinbach *et al.*, 2015). However, the most difficult part of such integration remains unsolved, *i.e.* preventing the occurrence of anti-phase domains, stacking faults and auto-diffusion of group IV elements in the grown structures (Morizane, 1977; Guo *et al.*, 2012; Dixit *et al.*, 2014; Koppka *et al.*, 2016; Galiana *et al.*, 2008; Bracht *et al.*, 2009; Aggarwal *et al.*, 2019; Roychowdhury *et al.*, 2019). In order to overcome the generation of stacking faults in the nano-structure of these materials, the tensile strain based (111) surface is preferred because it does not allow the glide of 90° partial dislocations and limits the nucleation kinetics of 60° dislocations (Kvam & Hull, 1993; Marée *et al.*, 1987). Therefore tensile strain based (111) hetero-structures can be an ideal combination for growing dislocation-free nanostructures

(Kvam & Hull, 1993). In support of the above methodologies, dislocation-free self-assembled tensile strained GaP dots have been grown on (111) oriented GaAs substrates (Simmonds & Lee, 2011). Recently, in another work, it was also reported that passivation of group IV substrates by the pre-layer of hydrides can hinder the formation of anti-phase domains while growing the III–V layer (Supplie, May, Kleinschmidt *et al.*, 2015). Further, it may be noted that (111) surfaces have the highest structural and piezoelectric field symmetry among the low-index crystallographic planes. Hence, tensile strained quantum dots grown on the (111) surface are expected to exhibit enhanced entangled photon emission in comparison with quantum dots grown on the (100) surface (Yerino *et al.*, 2014). Moreover, the presence of tensile strain also allows tunability to electronic states which helps to couple quantum information devices with existing fiber optics networks (Chen *et al.*, 2018). In addition, recent studies also suggest that tensile strained III–V semiconductor nanostructures grown on the (111) surface of Si and Ge have scope for being an efficient source of entangled photons (Benson *et al.*, 2000; Bayer *et al.*, 2002; Schliwa *et al.*, 2009; Singh & Bester, 2009). Also, among the III–V semiconductors, GaP is also regarded as one of the prime candidates for efficient detection of these entangled photons because of its high second-order nonlinear parameter, good thermal conductivity and broad transparency range (Anthur *et al.*, 2020; Rivoire *et al.*, 2009, 2011; Shambat *et al.*, 2010; Sanatinia *et al.*, 2012, 2014). Thus, GaP based tensile strained quantum dots or nanostructures grown on the (111) surface of Si and Ge would be one of the most suitable candidates for the above applications. In view of this, we have attempted to grow GaP nanostructures on Si and Ge (111) surfaces and investigated their detailed structural and optical properties (Roychowdhury *et al.*, 2017). It was observed that the high surface and interface energy difference among GaP and Ge (111) is advantageous for isolated and controlled nanostructure in comparison with GaP and Si (111) (Roychowdhury *et al.*, 2017). Therefore, it is anticipated from the above discussion that tensile strained GaP nanostructures on Ge (111) can be deployed for the development of quantum information technology. However, several growth challenges and inter-diffusion effects need to be addressed before the final design of the structure. Interestingly, the important factor of auto-diffusion of Si and Ge substrate materials on the grown III–V epitaxial structures are investigated to a lesser extent. Some of the work has reported that auto-diffused Si and Ge can occupy both the Ga and As sites in GaAs layers, grown by metal-organic vapor phase epitaxy (MOVPE) and molecular beam epitaxy (MBE), depending on the growth conditions (Dunlap Jr, 1954; Galiana *et al.*, 2008; Wang *et al.*, 2018; Gupta & Khokle, 1985). Also, by the increased amount of auto-diffusion of group IV elements into the III–V layer, the free carrier density starts reducing due to the charge carrier compensation. In a recent work, it was reported that auto-diffused Ge into GaAs epilayer acts as an n-type dopant when grown at 860°C. The dopant density due to Ge diffusion at high temperature (860°C) in GaAs can be very high, $\gg 10^{18}$ cm^{-3}. The thermal activation energy of the defect centers formed by the diffused Ge and the gallium vacancies (Ge_{Ga}–V_{Ga}) are estimated from configurational coordination modeling (Wang *et al.*, 2018). The auto-diffusion can be reduced by growing the barrier layer at low temperature, ~475°C, with reduced time duration of growth (Galiana *et al.*, 2008). Similarly, it is extremely important to understand the effect of Si and Ge auto-diffusion in GaP. There are few reports on the auto-diffusion of Si into GaP and GaAsP, while the role of Ge auto-diffusion into the GaP epilayer has not been investigated extensively (Andre *et al.*, 1975; Dixit *et al.*, 2008). Substitution of Ga atoms with Ge is more favorable compared with Si because the atomic radius of Ge is close to that of Ga (Vainshtein *et al.*, 2012, and references therein; Clementi & Raimondi, 1963). Additionally, the diffusion coefficient of Ge is higher than that of Si (Ogino *et al.*, 1982; Silvestri *et al.*, 2006; Greiner & Gibbons, 1984). Thus, by growing GaP on a Ge substrate, there is an extremely high possibility for Ge auto-diffusion into the GaP that may affect the local crystalline structure and generate strain in the grown epilayer. The auto-diffused Ge can replace either atomic sites or interstitial sites in the lattice of GaP depending on the activation energy of the Ge, Ga and P elements, which arises mainly due to the electronegativity differences between the elements.

In view of the above, the internal structural parameters of GaP/Ge(111) are evaluated. At first the inter-atomic distance, the strain state and structural coherency in the GaP nucleating and thick epilayers grown on Ge (111) are investigated by HRXRD. Subsequently, the auto-diffusion possibility of Ge in GaP is evaluated from the depth profile of Ga, P and Ge atoms by using secondary ion mass spectrometry (SIMS). The effect of Ga replacement by the Ge atom in the lattice is investigated by measuring the nature of the charge and its concentration from electrochemical capacitance voltage (ECV) measurements. Thereafter, the modification in the local structure of GaP due to the diffusion of Ge is investigated by polarization-dependent X-ray absorption spectroscopy (XAS) measurements. Finally, strain calculated at the atomic level from the variation in the bond lengths of Ga—P and Ga—Ga bonds are used to explain the residual strain distribution in the GaP epilayers grown on Ge (111).

2. Experimental details

Epitaxial layers of GaP were grown in a MOVPE reactor (AIX-200) at 20 mbar pressure, on Ge (111) substrate. Trimethyl gallium (TMGa) and phosphine (PH_3) were used as precursors for the growth of the GaP layers. The modified Radio Corporation of America (RCA) cleaning procedure was followed on the Ge (111) substrate prior to the growth, and the cleaned substrate was loaded into the MOVPE reactor. A high V/III ratio of ~1725 was maintained for growing the GaP nucleating layer of thickness ~60 nm at 425°C temperature, whereas a thick GaP layer of ~820 nm was grown using the two-step growth process at 770°C with the V/III ratio kept at 100. In this investigation, two sets of samples were used, referred to here as S_1 and S_2. Sample S_1

(nucleating layer) is island-type GaP with partial coverage of the Ge substrate (Roychowdhury *et al.*, 2017; Dixit *et al.*, 2014). Sample S_2 contains a nucleating layer of 60 nm at low temperature, 425°C, followed by a thick layer, ~760 nm, at a high temperature of 770°C. This growth process is referred to as the two-step growth process and detailed growth conditions are reported elsewhere (Dixit *et al.*, 2008, 2014; Navarro *et al.*, 2017; Koppka *et al.*, 2016; Volz *et al.*, 2011). Sample S_1 was grown for investigating the morphology, crystalline quality and other optical properties of the nucleation layer of GaP which precedes the growth of the thick layer. Also, the presence of defects like micro-twinning, anti-phase domains and other interfacial properties would be more prominent in S_1. Further, for obtaining the diffusion properties of Ge in GaP, it was necessary to have the thick layer sample S_2, especially to perform ECV and SIMS experiments. A PANalytical X'PERT diffractometer with Cu $K_{\alpha1}$ X-rays (λ = 1.5405 Å) with a hybrid 4X monochromator was used for the HRXRD measurements. SIMS measurements were also performed on S_2, in order to check for Ge diffusion within the GaP layer. The depth profiling in the GaP layer grown on Ge (111) was obtained by SIMS using a Cs^+ ion gun operated at 1 keV, 75 nA. Experiment and analysis were performed under a vacuum of $\sim10^{-9}$ mbar using Bi^{1+} ions operating at 30 keV, 4.7 pA. The area of analysis was 100 µm × 100 µm inside a sputter crater of 300 µm × 300 µm. Moreover, the site occupancy of the diffused Ge atom in the GaP layer was investigated by ECV measurements by a circular etched crater of 3 mm diameter. Further, to investigate the nearest neighbor atomic arrangement, X-ray absorption spectroscopy (XAFS) measurements were performed at the Ga *K*-edge using the scanning XAFS beamline (BL-9) at the INDUS-2 synchrotron source (Poswal *et al.*, 2016). XAFS measurements were performed in fluorescence mode using a vortex energy-dispersive detector. A Si (111) based double-crystal monochromator was used to select the excitation energy and an Rh/Pt-coated meridional cylindrical mirror for collimation in the beamline. The presence of residual strain in a relaxed layer of GaP grown on Ge (111) was further investigated from XAFS measurements. It is known that the X-ray beam in a synchrotron radiation source is linearly polarized and hence the residual strain distribution information for the in-plane and out-of-plane directions of the sample can be obtained (Figueroa *et al.*, 2016). Thus, polarization-dependent XAFS measurements were performed using two different sample mounting geometries. In one case the polarization vector is parallel to the growth direction and in the other case it is perpendicular to the growth direction that is used to probe the in-plane and out-of-plane bond lengths of the grown layer. The XAFS data are normalized and the background was subtracted using *ATHENA* software and then fitted using *ARTEMIS* software (Ravel & Newville, 2005).

3. Results and discussion

Figure 1 shows the HRXRD profile of S_1 and S_2 for various reflections. The two Bragg diffraction peaks in the $\omega/2\theta$ scan correspond to the GaP epilayer and Ge substrate, respectively. It is observed that the relative intensity of the GaP peak is higher for sample S_2 in comparison with S_1 which is predominantly due to its larger thickness [Figs. 1(*a*)–1(*d*)]. The presence of micro-twinning in S_1 and S_2 is identified from the φ scan [Figs. 1(*e*) and 1(*f*) show φ scans of S_1 and S_2]. From the relative intensity of the φ scans the extent of the micro-twin-

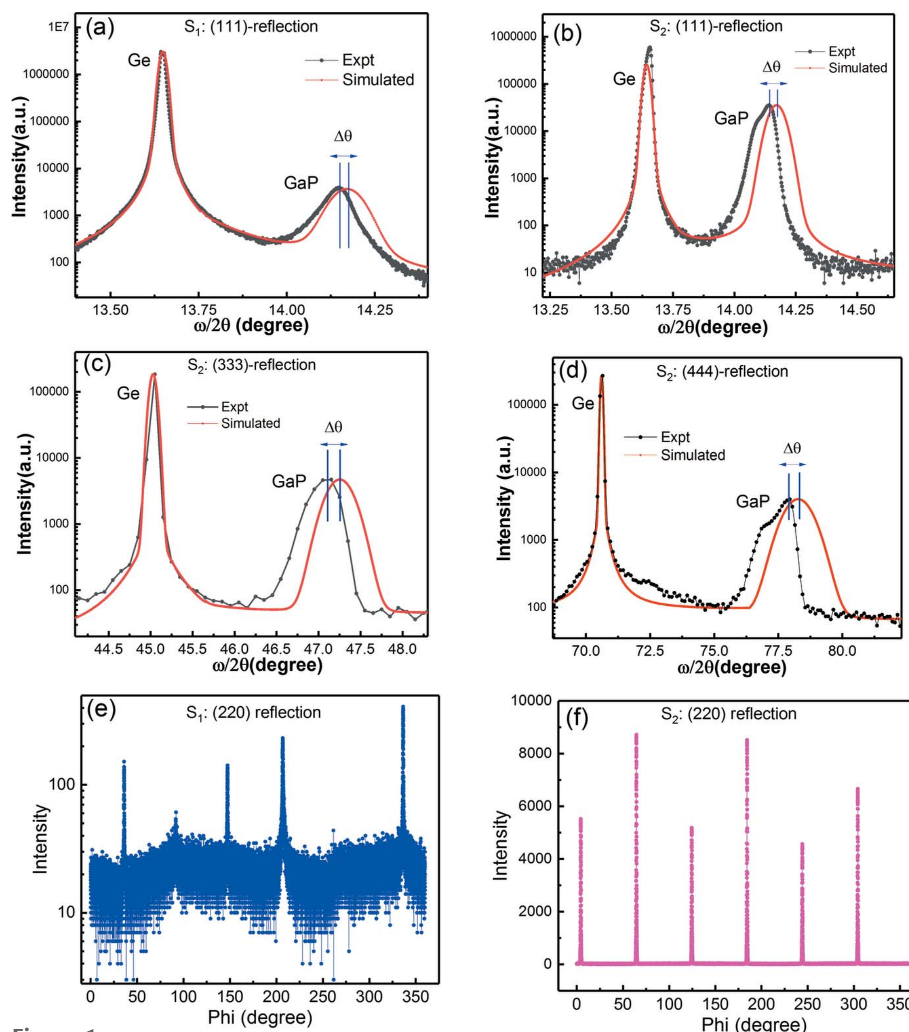

Figure 1
$\omega/2\theta$ scans of HRXRD for GaP/Ge(111) hetero-structures: (*a*) S_1 (111), (*b*) S_2 (111), (*c*) S_2 (333) and (*d*) S_2(444) reflections. φ scans of (*e*) S_1 and (*f*) S_2.

ning is estimated to be 32.24% and 39.43% for S_1 and S_2, respectively (Roychowdhury *et al.*, 2017; Koppka *et al.*, 2016). A detailed discussion on the φ scans of these samples has been reported earlier (Dixit *et al.*, 2014). Further, it is to be noted that the thickness of the GaP epilayers, in both S_1 and S_2, is much higher than the critical thickness of the GaP/Ge hetero-structure and hence it is expected that the layer relaxes via formation of defects/dislocations such as stacking faults, threading dislocations *etc.* The presence of these defects/dislocations causes a large amount of diffused scattering and broadening of the full width at half-maximum (FWHM) of the GaP diffraction peak. This also leads to a vanishing of the Pendellösung fringes which generally occurs in pseudo-morphic epilayers due to the coherent interference of diffracted X-rays from the layer and the substrates. The effects of these defects and dislocations are incorporated in the simulation of the HRXRD profile by considering diffused scattering and curvature of the sample. It may also be noted that under the pseudomorphic tensile strain condition the GaP diffraction peak can shift towards the *higher angle* (θ) compared with the completely relaxed layer due to the increased in-plane lattice constant and reduced out-of-plane lattice constant for the GaP/Ge hetero-structure. Moreover, as the thickness of the epilayers is higher than the critical thickness, it is anticipated that the diffraction peak position of GaP must overlap with the peak position of relaxed GaP epilayers of the simulated profile in S1 and S2. However, the experimentally measured GaP (111) diffraction peak is shifted by $\sim$80 and 72 arcsecond for S_1 and S_2, respectively [as shown in Figs. 1(*a*) and 1(*b*) and Table 1], towards the Ge substrate (*lower* θ) in comparison with the 100% relaxed GaP layer position (as determined from the simulated profile). This indicates the presence of residual strain within the GaP layer and its origin is different from the pseudomorphic strain condition. Further, GaP/GaAs has a similar lattice mismatch as that of GaP/Ge; however, for GaP when grown on GaAs substrate under similar growth conditions, such a shift of the GaP diffraction peak towards the substrate is not observed (Kumar *et al.*, 2016*b*). Thus this reconfirms that the origin of such residual strain is different than that caused by the pseudomorphic strain condition or the presence of defects and dislocations. Therefore, in order to investigate the origin of the observed residual strain, its quantitative value in the perpendicular direction for S_1 and S_2 is estimated from the following equation (Bassignana *et al.*, 1997; Singh *et al.*, 2016),

$$\varepsilon_{\perp} = \Delta\theta \cot\theta_{\rm B}, \quad (1)$$

where $\Delta\theta$ corresponds to the shift in the peak and $\theta_{\rm B}$ corresponds to the Bragg angle of GaP.

The estimated residual strain in the GaP layers for S_1 and S_2 is $\varepsilon = 1.41 \times 10^{-3}$ and $\varepsilon = 1.38 \times 10^{-3}$, as obtained from the peak separation of $\Delta\theta$ = 80 arcsecond and 72 arcsecond, respectively. This indicates that the order of residual strain is very similar irrespective of the thickness of the layer. In order to investigate the coherence nature of the residual strain in the grown layer, the diffraction profiles of multiple reflections including the (222), (333) and (444) reflections are examined.

Table 1
Residual strain values in samples S_1 and S_2 estimated from various crystallographic reflections of HRXRD.

Sample	Reflection	Shift, $\Delta\theta$ (arcsecond)	Bragg angle, $\theta_{\rm B}$ (°)	Residual strain, $\varepsilon \times 10^{-3}$
S_1	111	80	14.17	1.41
S_2	111	72	14.17	1.38
S_2	333	540	47.26	1.61
S_2	444	1440	78.26	1.45

Figures 1(*c*) and 1(*d*) show the diffraction profiles of the (333) and (444) reflections for S_2, while no diffraction peak is observed for the (222) reflection because of its systematic absence in GaP that arises from the structure factors. The shift in the Bragg diffraction peaks for various reflections due to the presence of residual strain are summarized in Table 1. It can be clearly seen from Figs. 1(*c*) and 1(*d*) and Table 1 that, although the corresponding peak shift in Bragg angle ($\theta_{\rm B}$) is higher for higher-order reflections, the calculated residual strain remains similar for all the reflections. It is confirmed that coherent residual strain is present in the GaP epilayers and it is tensile in nature along the growth direction with respect to the relaxed GaP layer. The origin of this residual strain may be due to the auto-diffusion of Ge from the substrate to the grown layer of GaP. This is due to the high diffusion co-efficient (2.11×10^{-22} cm^2 s^{-1}) of Ge in the GaP layer at the growth temperature (Ogino *et al.*, 1982; Silvestri *et al.*, 2006). The diffusion of Ge in GaP may change the lattice parameter and that can result in the shift of the Bragg diffraction peak of GaP towards Ge. Thus, it is essential to investigate the role of Ge diffusion in the structural, optical and electrical properties of the GaP layer, which is less explored (Dixit *et al.*, 2014). The residual strain may also occur due to the presence of micro-twinning and allotropes (wurtzite and zinc-blend phase) formation which has been observed from φ scans of HRXRD and Raman experiments (Aggarwal *et al.*, 2018; Dixit *et al.*, 2014). However, it has been reported that the micro-twinning fraction is largely reduced in the two-step growth process and becomes annihilated near the interface (Koppka *et al.*, 2016). Thus, the effect of this micro-twinning would be more prominent in S_1 (nucleating layer) compared with S_2. Although, it has been observed that the residual strain values are similar in both S_1 and S_2 (Table 1). This is a clear indication that the auto-diffusion of Ge may be the primary cause for the residual strain present in S_1 and S_2. Further, it is anticipated that residual strain due to micro-twinning would be different in different directions, while for our case it is observed that the residual strain remains coherent as determined from various symmetric and asymmetric reflections. Moreover, the presence of micro-twinning to a similar extent has also been observed for GaP/Si(111), but no signature of such residual strain has been observed for such samples (Roychowdhury *et al.*, 2017; Dixit *et al.*, 2006). Hence, from the above it can be concluded that Ge auto-diffusion within the GaP epilayer is the predominant cause for the residual strain present in samples S_1 and S_2.

Moreover, to estimate the extent of Ge diffusion within the GaP layer, SIMS measurement were performed on S_2 (thick layer of GaP). Considering a uniform etching rate the *x*-axis has been converted from sputtering time to depth scale. Figure 2(*a*) shows the depth profile of the Ge, Ga and P atoms in GaP/Ge hetero-structure obtained from the SIMS measurement. It is to be noted that the Bi^{1+} ions used for analysis are more sensitive to Ge compared with Ga and P. Therefore the maximum intensity has been normalized to 1 for Ga, P and Ge. However, the detection limits of the elements may vary as one moves from the GaP to the Ge matrix and thus direct comparison of the relative intensity in the epilayer and the substrate is complex (Ostheim *et al.*, 2019). From the SIMS profile it is observed that Ge is present throughout the GaP layer up to the top surface due to the high diffusion coefficient of Ge. Also the concentration of Ge decreases slowly up to a depth of 400 nm and then increases and saturates at a certain depth. On the other hand the concentration of Ga and P decreases very slowly up to a depth of about 400 nm, beyond which the concentration decreases at a comparatively higher rate and gradually becomes zero. Note that the GaP thick layer is grown over the island type nucleating layer and therefore surface roughness of the grown layer is high as observed in the atomic force microscopy image (Roychowdhury *et al.*, 2017). Therefore, the Cs^+ ion gun probes a large surface area at the top of the GaP/Ge hetero-structure. As the ion gun probes the inner depth of the hetero-structure, the interacting area may decrease and hence the concentration of Ga, P and Ge decreases at a very slow rate. After a certain depth of approximately 400 nm, the contribution from the buried island region of the GaP structure becomes more significant in the SIMS and ECV measurements. Thus, beyond 400 nm the concentration of Ga and P decreases at a faster rate while the Ge concentration increases until the substrate is reached. Further, the non-uniform diffusion of Ge within the GaP epilayer is expected to cause variation in the density of the GaP epilayer with depth. This density variation may also cause variation in the SIMS profile of Ga and P. But it is observed that the intensity of Ga and P vary similarly, independent of the Ge intensity profile. This is because the amount of diffused Ge atoms is $<5\%$, as estimated from the linear Vegard's law for GaPGe alloy and the relative diffraction peak positions observed by HRXRD. Thus we are not able to observe a detectable variation in the density of the epilayer in the SIMS profile of Ga and P.

The diffused Ge atom may occupy either or both the Ga and P atom sites or may accommodate itself in an interstitial position. It is reported that Ge replaces the gallium site in GaAs epilayer when grown at low temperature (Galiana *et al.*, 2008). This is mainly due to the similar atomic radii for the Ge and Ga atoms. Therefore, it is anticipated that the Ge atom may also replace the Ga sites in the GaP layer. The Ga replacement by the Ge atom in the lattice may increase the electron donor density in the conduction band. In order to estimate the charge density in the GaP epilayer, ECV measurements are performed. The calibrated ECV profile is shown in Fig. 2(*b*). It is observed that the GaP epilayer shows

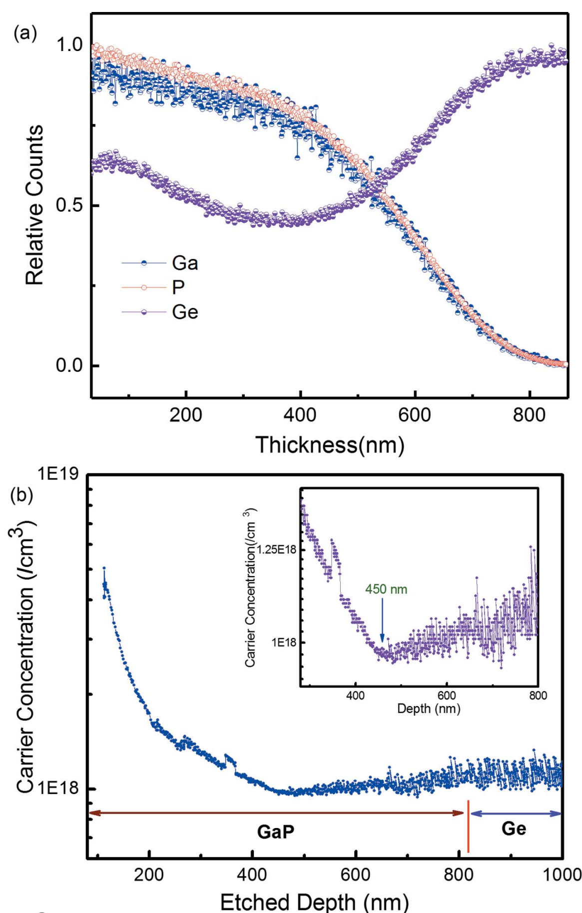

Figure 2
(*a*) Concentration profile of Ge, Ga and P atoms with depth in the GaP epilayer obtained from SIMS. (*b*) Depth profile of charge carrier density in the GaP epilayer measured from ECV. The dip observed in the ECV profile is shown in the inset of the figure.

n-type behavior with electron density $>10^{18}$ cm^{-3} at room temperature. This indicates that the probability of Ge atom replacement into the Ga atom site or into an interstitial position is high because it can naturally cause n-type behavior of the GaP layer. Further, the growth temperature is $<770°C$ and there is no signature of p-type nature of the layer. Therefore, it reduces the possibility of P atom replacement by the Ge atom within the lattice.

Further, recently Ostheim *et al.* reported that the presence of anti-phase domains (APDs) leads to an increase in conductivity of GaP epilayers grown on Si (001) substrate (Ostheim *et al.*, 2019). Thus, even for our structures (S_1 and S_2) the presence of APDs or micro-twinning may affect the carrier concentration of the epilayer. However, contributions of the anti-phase domain or micro-twinning in the conductivity are predominant at the interfacial layer of the hetero-structures, as also observed by Ostheim *et al.* As the thickness increases, the anti-phase domains and micro-twinnings are almost annihilated. It may be noted that the thicknesses of the epilayer in GaP in samples S_1 and S_2 are large, hence contributions of the interfacial layer dominated by the anti-phase domains and micro-twinning would be less at the top of the sample. In order to take care of parallel layer conduction, we

have preferred ECV over Hall experiments. ECV experiments were performed on a thick layer by making ohmic contact from the top of the epilayer and therefore initial data are almost free from the anti-phase domain or micro-twinning. As we move closer to the interfacial layer some of the effects may be visible in the data. However, it is observed that the order of carrier concentration remains at 10^{18} cm^{-3} throughout the epilayer. Thus the dopant density observed in the ECV measurements is mainly due to diffused Ge replacing the Ga lattice or interstitial sites. Moreover, it is also observed that the carrier concentration reduces up to a depth of about 400 nm and then slightly increases and saturates at a certain value. The inset of Fig. 2(*b*) clearly shows the dip region in the charge density profile. This result corroborates with the SIMS profile and reconfirms that beyond 400 nm thickness from the top of the surface the contribution from the island region of the structures becomes significant. Therefore, it is concluded from the SIMS and ECV profile that Ge is diffused in the GaP layer, predominantly occupying Ga atom or interstitial sites which is the prime cause of residual strain in the GaP/Ge system. It may also be noted in the SIMS profile that beyond 700 nm from the top surface the concentrations of Ga and P are reduced completely to the background. This indicates that the diffusion of Ga or P into the Ge substrate is not very significant because of the lower diffusion co-efficient of Ga and P within Ge. However, from Raman spectroscopy investigations, the signature of phosphorus diffusion within the Ge substrate is observed up to a thickness of 20 nm for the nucleating layer (S_1) leading to a red shift of 3.5 cm^{-1} and an increase in the FWHM of the optical phonon mode of Ge (Aggarwal *et al.*, 2019). On the other hand, the thick layer grown in the two-step process does not show the presence of phosphorus in the germanium substrate. This is because, at the thick layer growth temperature, phosphorus is desorbed from the germanium. This observation is confirmed by restoring the crystalline quality of Ge in the nucleating layer by thermal treatment at 700°C (Aggarwal *et al.*, 2019).

In order to investigate the effect of Ge atom diffusion on the local structure of the GaP epilayer, polarization-dependent XAFS measurements were performed for sample S_1. The linearly polarized beam of the synchrotron source is used to probe the in-plane and out-of-plane bond lengths by selecting two different sample mounting geometries as shown in Figs. 3(*a*) and 3(*b*). The measured data in the above geometries were normalized using *ATHENA* software and fitted by using the EXAFS equation in the *ARTEMIS* software (Ravel & Newville, 2005). The normalized data in the real space were Fourier transformed to the *k*-space in the *k*-range 3–9 Å^{-1}, and the obtained k^2-weighted $\chi(k)$ spectra of S_1 in the two different geometries along with that of GaP wafer are shown in Fig. 3(*c*). The data were fitted in the *k*-range 3–9 Å^{-1} using the standard EXAFS equation,

$$\chi(k) = \sum_j \frac{N_j S_0^2 f_j(k) \exp\left[-2R_j/\lambda(k)\right] \exp\left[-2k^2\sigma_j^2\right]}{kR_j^2} \times \sin\left[2kR_j + \delta_j(k)\right]. \quad (2)$$

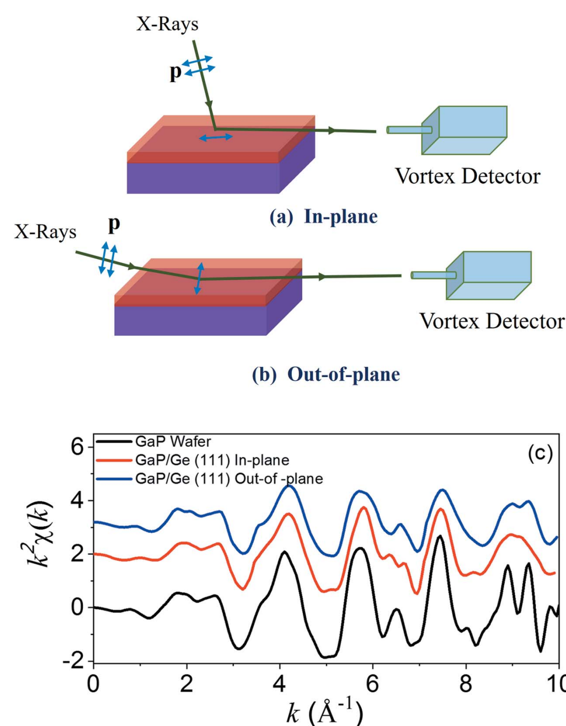

Figure 3
Schematic of the polarization-dependent XAFS measurement configurations (*a*) in-plane and (*b*) out-of-plane. (*c*) Experimental data of XAFS in k^2-weighted $\chi(k)$ showing the oscillations in *k*-space.

The standard parameters used for fitting are S_0 (amplitude reduction factor), N_j (number of nearest neighbors), R_j (bond length) and σ_j (Debye–Waller factor). The fitting was performed using GaP zinc blende structure with a space group of $F\bar{4}3m$. Moreover, among the above-mentioned parameters, by keeping N_j fixed the experimental fitting is better in comparison with variable N_j. The fitting results with fixed N_j indicate that the possibility of a diffused Ge atom occupying the Ga atom sites is predominant compared with the interstitial position. From this model and results of the ECV measurement it is conclusive that a diffused Ge atom in the GaP epilayer replaces the Ga sites making it n-type in nature. Figures 4(*a*) and 4(*b*) show the magnitude and real components of experimental and fitted $\chi(R)$ in real space coordinates (R_j) in the range 1–4.52 Å for sample S_1 (phase uncorrected) in two different geometries along with GaP wafer. The results of best fit values of the bond lengths and the Debye–Waller factors for GaP wafer and sample S_1 in two different geometries are listed in Table 2. The estimated bond length of the first, second and third nearest neighbor of the Ga atom for GaP wafer are 2.353 Å, 3.684 Å and 4.552 Å, respectively. Here the first nearest neighbor of Ga bonds with 4 P atoms (Ga—P1), the second next near-neighbor of Ga is surrounded by 12 Ga atoms (Ga—Ga1) and the third next near-neighbor of Ga is surrounded by 12 P atoms (Ga—P2). Figure 5 shows the atomic arrangement of Ga along with its first, second and third nearest neighbor (not shown) atoms in GaP structures. These bond length values closely match with the reported values of ZB–GaP structure (Schnohr *et al.*, 2008).

Table 2
Ga—P bond lengths in GaP wafer and GaP/Ge(111) hetero-structures, in the in-plane and out-of-plane geometry determined from XAFS fitting; the digits in the parentheses represent the error in fitting in the last decimal place of the bond length.

Sample	R_{Ga-P1} (Å)	σ^2_{Ga-P1} (Å^2)	R_{Ga-Ga1} (Å)	σ^2_{Ga-Ga1} (Å^2)	R_{Ga-P2} (Å)	σ^2_{Ga-P2} (Å^2)	*R*-factor
GaP wafer	2.353 (3)	0.0031 (4)	3.684 (4)	0.0043 (5)	4.552 (6)	0.0044 (7)	0.001
GaP/Ge(111) in-plane	2.338 (2)	0.0064 (2)	3.661 (4)	0.0117 (5)	4.557 (9)	0.0139 (5)	0.001
GaP/Ge(111) out-of-plane	2.351 (4)	0.0033 (6)	3.743 (9)	0.0101 (9)	4.555 (8)	0.0074 (8)	0.002

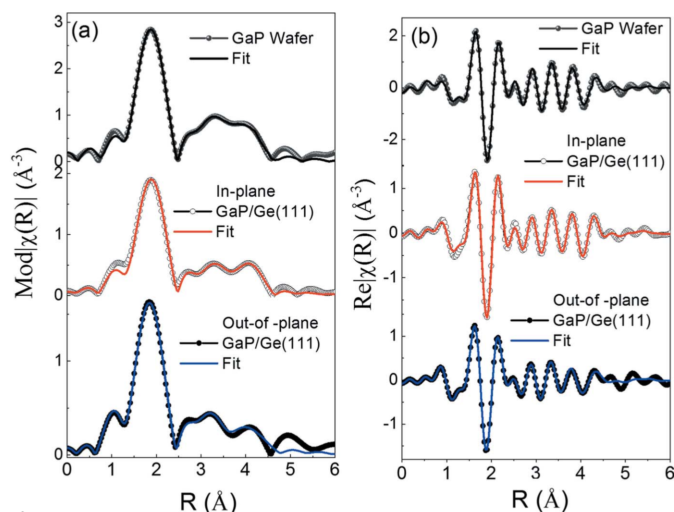

Figure 4
(*a*) Magnitude and (*b*) real components of experimental data of $\chi(R)$ with fittings in real space.

Thereafter, a similar procedure is used for the estimation of bond lengths of the first, second and third nearest neighbor of the Ga atom for the GaP epilayer (S_1). These estimated bond length values are 2.338 Å, 3.661 Å and 4.557 Å, respectively, for in the in-plane geometry and 2.351 Å, 3.743 Å and 4.555 Å for the out-of-plane geometry. It is observed from the results for the in-plane geometry that the first (Ga—P1) and second (Ga—Ga) nearest neighbor bond lengths in the epilayer are reduced in comparison with GaP wafer. On the other hand, for the out-of-plane geometry the bond lengths Ga—P1 remain identical while Ga—Ga shows distinct changes in the epilayer in comparison with GaP wafer. The origin of bond length variations in the GaP epilayer is explained by considering that the scattering contribution of a particular nearest neighbor atom in the EXAFS signal is proportional to $3\cos^2(\alpha)$, where α is the angle between the bond vector and the direction of polarization (Tormen *et al.*, 2001). For zinc blend structure, assuming one of the Ga sites to be the origin and the reference frame shown in Fig. 3(*c*), the four bond vectors of the first nearest neighbor (Ga—P1) can be written as $\mathbf{R}_1 = a/4(1,1,1)$, $\mathbf{R}_2 = a/4(-1,-1,1)$, $\mathbf{R}_3 = a/4(-1,1,-1)$ and $\mathbf{R}_4 = a/4(1,-1,-1)$ where a represents the lattice constant (Tormen *et al.*, 1999). Note that among these four vectors $[\mathbf{R}_1]$ makes an angle of 0° with the normal ($\mathbf{n}$) to the growth direction (111) and the vectors $[\mathbf{R}_2, \mathbf{R}_3, \mathbf{R}_4]$ make an angle of approximately 70.53° with $\mathbf{n}$. Moreover, for the in-plane geometry the polarization vector ($\mathbf{p}$) is in the growth plane of the layer and that makes an angle of 90° with $\mathbf{n}$, whereas for the out-of-plane geometry $\mathbf{p}$ is parallel to $\mathbf{n}$. Therefore, for the vector $[\mathbf{R}_1]$, α is 90° for the in-plane geometry and 0° for the out-of-plane geometry. On the other hand, for the vectors $[\mathbf{R}_2, \mathbf{R}_3, \mathbf{R}_4]$, α is 19.47° for the in-plane geometry and 70.53° for the out-of-plane geometry. Hence, we can infer that, for the (111) growth direction, among the first nearest neighbors, the contribution of $[\mathbf{R}_2, \mathbf{R}_3, \mathbf{R}_4]$ will be dominant for the in-plane geometry and $[\mathbf{R}_1]$ will have a dominant contribution for the out-of-plane geometry. A similar procedure can be applied for the 12 second nearest neighbors (Ga—Ga) and the constructed bond vectors can be written as $\mathbf{R}_1 = a/2(1,1,0)$, $\mathbf{R}_2 = a/2(-1,1,0)$, $\mathbf{R}_3 = a/2(-1,-1,0)$, $\mathbf{R}_4 = a/2(1,-1,0)$, $\mathbf{R}_5 = a/2(1,0,1)$, $\mathbf{R}_6 = a/2(-1,0,1)$, $\mathbf{R}_7 = a/2(1,0,-1)$, $\mathbf{R}_8 = a/2(-1,0,-1)$, $\mathbf{R}_9 = a/2(0,1,1)$, $\mathbf{R}_{10} = a/2(0,-1,1)$, $\mathbf{R}_{11} = a/2(0,1,-1)$, $\mathbf{R}_{12} = a/2(0,-1,-1)$. Among these vectors $[\mathbf{R}_2, \mathbf{R}_4, \mathbf{R}_6, \mathbf{R}_7, \mathbf{R}_{10}, \mathbf{R}_{11}]$ makes an

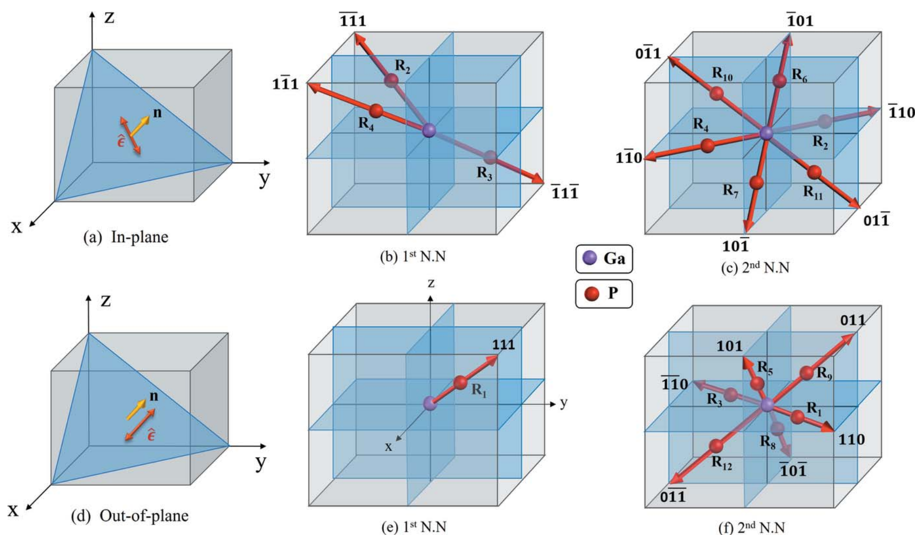

Figure 5
(*a*) Reference frame showing the polarization vector ($\hat{\epsilon}$) for in-plane geometry. (*b*) First nearest neighbor bond vectors that dominantly contribute in the in-plane geometry ($\mathbf{R}_2, \mathbf{R}_3, \mathbf{R}_4$). (*c*) Second nearest neighbor bond vectors that dominantly contribute in the in-plane geometry ($\mathbf{R}_2, \mathbf{R}_4, \mathbf{R}_6, \mathbf{R}_7, \mathbf{R}_{10}, \mathbf{R}_{11}$). (*d*) Reference frame showing the polarization vector ($\hat{\epsilon}$) for out-of-plane geometry. (*e*) First nearest neighbor bond vectors that dominantly contribute in the out-of-plane geometry ($\mathbf{R}_1$). (*f*) Second nearest neighbor bond vectors that dominantly contribute in the out-of-plane geometry ($\mathbf{R}_1, \mathbf{R}_3, \mathbf{R}_5, \mathbf{R}_8, \mathbf{R}_9, \mathbf{R}_{12}$).

angle of 90° with **n** and vectors [$\mathbf{R}_1$, $\mathbf{R}_3$, $\mathbf{R}_5$, $\mathbf{R}_8$, $\mathbf{R}_9$, $\mathbf{R}_{12}$] make an angle of 35.26° with **n**. Thus for vectors [$\mathbf{R}_2$, $\mathbf{R}_4$, $\mathbf{R}_6$, $\mathbf{R}_7$, $\mathbf{R}_{10}$, $\mathbf{R}_{11}$] α is 0° in the in-plane geometry and 90° in the out-of-plane geometry. Hence this subset of second nearest neighbors will have a dominant contribution in the in-plane geometry. On the other hand, for the vectors [$\mathbf{R}_1$, $\mathbf{R}_3$, $\mathbf{R}_5$, $\mathbf{R}_8$, $\mathbf{R}_9$, $\mathbf{R}_{12}$] α is 54.74° in the in-plane geometry and 35.26° in the out-of-plane geometry. Therefore this subset will have a two times larger contribution in the out-of-plane geometry. The bond vectors of the first and second nearest neighbor contributing dominantly in the in-plane and out-of-plane EXAFS data are separately shown in Fig. 5. Thus, the above discussion suggests that for the first and second nearest neighbors of zinc blende structure the bonds which are dominantly contributing in the in-plane and out-of-plane geometries of the EXAFS data are different. Hence, the reduction in bond length of the first and second nearest neighbor for the GaP epilayer with respect to the GaP wafer in the in-plane geometry indicates that the length of the bond vectors, dominantly contributing in the in-plane geometry, has decreased. On the contrary, the length of the bond vectors dominantly contributing in the out-of-plane geometry has increased, which leads to an increase in the bond length of the GaP epilayer in the out-of-plane geometry.

This difference in bond length of the first and second nearest neighbor between GaP wafer and epilayer is another indication of residual strain in the GaP epilayer due to the presence of diffused Ge as indicated in the SIMS and ECV results. However, as mentioned earlier, the epilayers of GaP in S_1 and S_2 are relaxed via the formation of defects and dislocations. The presence of these defects and dislocations may also cause variation of local bond length in the GaP epilayer for S_1 and S_2. Therefore, in order to confirm the origin of this variation in the local bond length we have calculated the dislocation density present in S_1 and S_2 from the FWHM of the rocking curve of these samples. The rocking curve of these samples has been reported previously (Dixit *et al.*, 2014). The dislocation density is given by (Yarlagadda *et al.*, 2008)

$$D = \frac{(\mathrm{FWHM})^2}{9b^2}$$

where FWHM is the full width at half-maximum of the rocking curve and b corresponds to the magnitude of the Burgers vector. It is known that for the (111) growth direction the propagation of dislocation is also along the (111) direction and thus we considered the (111) reflection of the rocking curve for our calculation. The FWHM of S_1 and S_2, determined from the rocking curve, are 0.211° and 0.213°, respectively, and the magnitude of the Burgers vector is assumed to be $a/3\langle 111\rangle$ (Oktyabrsky, 2001). By considering these values the dislocation density for S_1 and S_2 are estimated to be 1.52×10^9 cm^{-2} and 1.55×10^9 cm^{-2}, respectively. It may be noted that the charge carrier density in the GaP epilayer estimated from ECV measurements was 10^{18} cm^{-3}. This indicates that the typical number of Ge atoms present in a unit plane could be 10^{12} cm^{-2} which is three orders of magnitude larger than the dislocation density. Therefore it may be anticipated that the contribution of the diffused Ge atom on the variation of the bond length would be much higher compared with the presence of defects and dislocations in the epilayers.

Moreover, the anisotropic behavior of the bond length indicates that the nature of residual strain in the epilayer is different for the in-plane and the out-of-plane directions. It may also be noted that the bond length of the third nearest neighbor of the Ga atom, Ga—P2, remains almost equal in both the geometries for the epilayer and wafer. Here, the difference in the bond length between the epilayer and wafer is indistinguishable due to the reduced strength of the experimental data in the higher k region and therefore less accuracy in the fitting. Thus the presence of residual strain effects is not evident in the third nearest neighbor of the Ga atom, Ga—P2. The presence of this residual tensile strain finally led to a shift in the diffraction peak towards lower diffraction angle as observed in all the reflections of the HRXRD. Therefore, the variation in the bond lengths values of the Ga—P and Ga—Ga atoms are used to determine the strain distribution for the in-plane and the out-of-plane directions. For the zinc blende structure, under the tetragonal distortion and Poisson's effect, the macroscopic strain present in a system is related to the microscopic variation in the bond length for the first nearest neighbor by the equation (Romanato *et al.*, 1998; Lamberti, 2004)

$$\frac{\delta r_{\rm IC}^{\rm st}}{a} = \frac{(2-\gamma)}{4\sqrt{3}}\,\varepsilon_{\parallel} \tag{3}$$

where $\delta r_{\rm IC}^{\rm st}$ is the variation in the bond length of the first nearest neighbor, a corresponds to the lattice constant, γ corresponds to Poisson's ratio and ε corresponds to the strain present in the system. Moreover, the above equation is also valid for relaxed layers which is the case of the GaP epilayer grown on Ge (Tormen *et al.*, 1999). The difference between the in-plane bond lengths of the wafer and epilayer ($\delta r_{\rm IC}^{\rm st}$) is -0.015 Å, where the negative sign indicates reduction and this value is used to estimate residual strains. The estimated strain values of $\varepsilon_{\perp}$ and $\varepsilon_{\parallel}$ are 3.5×10^{-3} and -11.282×10^{-3}, respectively. Here the Poisson's ratio value of 0.31 is used for estimating the out-of-plane strain using the expression $\varepsilon_{\perp} = -\gamma\varepsilon_{\parallel}$ (Romanato *et al.*, 1998). It may also be noted that the exact value of $\varepsilon_{\perp}$ (3.5×10^{-3}) calculated from equation (3) is higher than that estimated (1.38×10^{-3}) from HRXRD. In view of this difference, the relation between variations in local bond length with macroscopic strain is further extended for the second nearest neighbor and they are related as (Tormen *et al.*, 2001)

$$\frac{\delta r_{\rm 2nd}^{\rm in}}{a} = \frac{\varepsilon_{\parallel}}{\sqrt{2}} \tag{4}$$

where $\delta r_{\rm 2nd}^{\rm in}$ is the difference between the in-plane bond length of the GaP epilayer and wafer. By using the value of $\delta r_{\rm 2nd}^{\rm in} = -0.023$ Å in the above equation and the Poisson effect, $\varepsilon_{\perp}$ and $\varepsilon_{\parallel}$ are estimated to be 1.85×10^{-3} and -5.97×10^{-3}, respectively. Now the magnitude of $\varepsilon_{\perp}$ closely matches the residual strain estimated from HRXRD. This is because by considering the higher-order nearest neighbor we are moving from the microscopic to the macroscopic level. The magnitude

of $\varepsilon_\perp$ and $\varepsilon_\parallel$, calculated from the distortion in bond length of the first and second nearest neighbors, explains the shift of the GaP diffraction peak toward the Ge substrate Bragg diffraction peak observed in HRXRD. Further, from the sign of $\varepsilon_\perp$ and $\varepsilon_\parallel$, it is confirmed that the nature of the residual strain for the out-of-plane case is tensile while for the in-plane case it is compressive. Thus it can be concluded that variation in the bond length of the first and second nearest neighbor of the Ga atom in the GaP epilayer can effectively be utilized for determining the magnitude and direction of the strain which can be correlated with residual strain estimated from HRXRD. The corroboration between the residual strain calculated from the difference in bond length and the residual strain calculated from the shift in the HRXRD peak reconfirms that the variation in bond length of GaP in S_1 is primarily caused by Ge diffusion within the GaP epilayer.

4. Conclusion

The effects of Ge auto-diffusion into GaP epitaxial layers on the inter-atomic distance and the bond length of Ga and P are investigated by using high-resolution X-ray diffraction and X-ray absorption spectroscopy. It is observed that the diffraction peak of GaP shifts towards Ge from the relaxed position of bulk GaP and the shift varies from 78 to 1440 arcseconds for various reflections, which indicates the presence of residual strain within the relaxed epilayer leading to change in the inter-planar atomic distance. The impact of polar/non-polar and lattice mismatch, leading to formation of micro-twins and the dislocation/defect within the GaP epilayer, are estimated from $\omega/2\theta$, ω and φ scans. Their contributions are incorporated by considering the diffused scattering in the HRXRD; as a result, the simulated profile matches closely with the experimental data. Subsequently, the magnitude of the coherent residual strain, in the relaxed GaP epilayer, is estimated. It is also concluded from the investigation of SIMS and ECV that the Ge auto-diffusion, leading to the substitution of Ga or interstitial sites, is the predominant source of the residual strain. Subsequently, the local variation of Ga inter-atomic distances, due to the presence of residual strain, is investigated by the polarization-dependent XAFS measurements in two different sample mounting geometries that are performed for distinguishing the in-plane and out-of-plane bond lengths of the Ga neighbors in the grown layer. The estimated bond lengths of the first, second and third nearest neighbors of the Ga atom for the GaP epilayer are 2.338 Å, 3.661 Å and 4.557 Å, respectively, for the in-plane geometry and 2.351 Å, 3.743 Å and 4.555 Å for the out-of-plane geometry. These bond length values estimated by fitting the XAFS data are used for evaluating the microscopic residual strain and are correlated with the macroscopic strain. The magnitude of $\varepsilon_\perp$ and $\varepsilon_\parallel$ calculated from the distortion in bond length of the first and second nearest neighbors explains the shift of the GaP Bragg diffraction peak towards the Ge substrate. Further, from the sign of $\varepsilon_\perp$ and $\varepsilon_\parallel$, it is confirmed that the nature of the residual strain is tensile in the out-of-plane direction and compressive in the in-plane direction. Moreover, it is observed that by considering higher-order nearest neighbors the value of the residual strain determined from XAFS matches well with that determined from HRXRD. Thus it can be concluded that the variation in bond length of the first and second nearest neighbor of the Ga atom in the GaP epilayer can be utilized for determining the magnitude and direction of the microscopic residual strain which can be correlated with the strain estimated from HRXRD. The modified nearest neighbor configurations of Ga in the GaP epilayer due to diffused Ge are proposed for new possibilities within the GaP/Ge (111) hetero-structures. It has been reported that Ge—P forms stronger bonding and the degree of disorder and anti-site defects can enable the bandgap tuning from its equilibrium values (Pham *et al.*, 2020). Thus, such an auto-diffusion under controlled conditions can be used in the conversion from indirect to direct band structures similar to the recently reported GaPN and WZ Si in $Si_{1-x}Ge_x$ alloys (Fadaly *et al.*, 2020) and engineering the tensile strain quantum dot structures on (111) surfaces.

Acknowledgements

The authors acknowledge Shri U. K. Ghosh and Shri A. Khakha for the technical support during the MOVPE growth and Shri Subhomoy Haldar, Ms Geetanjali Vashisht, Ms Preeti Pokhriyal and Dr Tapas Ganguli for useful scientific discussions. The authors also acknowledge Shri S. V. Nakhe, group director, and Shri D. Das, Director RRCAT, for their constant support during the course of this work.

Funding information

RR would like to thank HBNI-India for providing a research fellowship.

References

Aggarwal, R., Ingale, A. A. & Dixit, V. K. (2018). *Appl. Surf. Sci.* **427**, 754–762.
Aggarwal, R., Ingale, A. A., Dixit, V. K. & Sathe, V. (2019). *Superlattice Microstruct.* **125**, 190–197.
Andre, J., Hallais, J. & Schiller, C. (1975). *Vapour Growth and Epitaxy*, pp. 147–157. Elsevier.
Anthur, A. P., Haizhong, Z., Akimov, Y., Junrong, O., Kalashnikov, D., Kuznetsov, A. I. & Krivitsky, L. (2020). *arXiv*: 2001.06142.
Bassignana, I., Macquistan, D., Streater, R., Hillier, G., Packwood, R. & Moore, V. (1997). *J. Cryst. Growth*, **172**, 25–36.
Bayer, M., Ortner, G., Stern, O., Kuther, A., Gorbunov, A., Forchel, A., Hawrylak, P., Fafard, S., Hinzer, K., Reinecke, T., Walck, S. N., Reithmaier, J. P., Klopf, F. & Schäfer, F. (2002). *Phys. Rev. B*, **65**, 195315.
Benson, O., Santori, C., Pelton, M. & Yamamoto, Y. (2000). *Phys. Rev. Lett.* **84**, 2513–2516.
Bracht, H., Schneider, S., Klug, J., Liao, C., Lundsgaard Hansen, J., Haller, E., Nylandsted Larsen, A., Bougeard, D., Posselt, M. & Wündisch, C. (2009). *Phys. Rev. Lett.* **103**, 255501.
Chen, S., Li, W., Wu, J., Jiang, Q., Tang, M., Shutts, S., Elliott, S. N., Sobiesierski, A., Seeds, A. J., Ross, I., Smowton, P. M. & Liu, H. (2016). *Nat. Photon.* **10**, 307–311.
Chen, Y., Zopf, M., Keil, R., Ding, F. & Schmidt, O. G. (2018). *Nat. Commun.* **9**, 2994.
Clementi, E. & Raimondi, D.-L. (1963). *J. Chem. Phys.* **38**, 2686–2689.

Dixit, V. K., Ganguli, T., Sharma, T. K., Kumar, R., Porwal, S., Shukla, V., Ingale, A., Tiwari, P. & Nath, A. (2006). *J. Cryst. Growth*, **293**, 5–13.
Dixit, V. K., Ganguli, T., Sharma, T. K., Singh, S. D., Kumar, R., Porwal, S., Tiwari, P., Ingale, A. & Oak, S. M. (2008). *J. Cryst. Growth*, **310**, 3428–3435.
Dixit, V. K., Kumar, S., Singh, S. D., Khamari, S. K., Kumar, R., Tiwari, P., Phase, D. M., Sharma, T. K. & Oak, S. M. (2014). *Appl. Phys. Lett.* **104**, 092101.
Dunlap, W. Jr (1954). *Phys. Rev.* **94**, 1531–1540.
Fadaly, E. M., Dijkstra, A., Suckert, J. R., Ziss, D., van Tilburg, M. A., Mao, C., Ren, Y., van Lange, V. T., Korzun, K., Kölling, S., Verheijen, M. A., Busse, D., Rödl, C., Furthmüller, J., Bechstedt, F., Stangl, J., Finley, J. J., Botti, S., Haverkort, J. E. M. & Bakkers, E. P. A. M. (2020). *Nature*, **580**, 205–209.
Figueroa, A., Zhang, S., Baker, A., Chalasani, R., Kohn, A., Speller, S., Gianolio, D., Pfleiderer, C., van der Laan, G. & Hesjedal, T. (2016). *Phys. Rev. B*, **94**, 174107.
Galiana, B., Rey-Stolle, I., Algora, C., Volz, K. & Stolz, W. (2008). *Appl. Phys. Lett.* **92**, 152102.
Grassman, T., Carlin, J., Galiana, B., Yang, L.-M., Yang, F., Mills, M. & Ringel, S. (2013). *Appl. Phys. Lett.* **102**, 142102.
Greiner, M. E. & Gibbons, J. F. (1984). *Appl. Phys. Lett.* **44**, 750–752.
Guo, W., Bondi, A., Cornet, C., Létoublon, A., Durand, O., Rohel, T., Boyer-Richard, S., Bertru, N., Loualiche, S., Even, J. & Le Corre, A. (2012). *Appl. Surf. Sci.* **258**, 2808–2815.
Gupta, R. & Khokle, W. (1985). *Solid-State Electron.* **28**, 823–830.
Koppka, C., Paszuk, A., Steidl, M., Supplie, O., Kleinschmidt, P. & Hannappel, T. (2016). *Cryst. Growth Des.* **16**, 6208–6213.
Kumar, R., Dixit, V. K., Ganguli, T., Mukherjee, C., Srivastava, A. & Sharma, T. K. (2016*b*). *J. Appl. Phys.* **120**, 135307.
Kumar, R., Dixit, V. K., Sinha, A. K., Ganguli, T., Mukherjee, C., Oak, S. M. & Sharma, T. K. (2016*a*). *J. Synchrotron Rad.* **23**, 238–243.
Kvam, E. & Hull, R. (1993). *J. Appl. Phys.* **73**, 7407–7411.
Lamberti, C. (2004). *Surf. Sci. Rep.* **53**, 1–197.
Liebich, S., Zimprich, M., Beyer, A., Lange, C., Franzbach, D., Chatterjee, S., Hossain, N., Sweeney, S., Volz, K., Kunert, B. & Stolz, W. (2011). *Appl. Phys. Lett.* **99**, 071109.
Marée, P., Barbour, J., van der Veen, J., Kavanagh, K., Bulle–Lieuwma, C. & Viegers, M. (1987). *J. Appl. Phys.* **62**, 4413–4420.
Morizane, K. (1977). *J. Cryst. Growth*, **38**, 249–254.
Navarro, A., García-Tabarés, E., Galiana, B., Caño, P., Rey-Stolle, I. & Ballesteros, C. (2017). *J. Cryst. Growth*, **464**, 8–13.
Ogino, M., Oana, Y. & Watanabe, M. (1982). *Phys. Status Solidi A*, **72**, 535–541.
Oktyabrsky, S. (2001). *Encyclopedia of Materials: Science and Technology*, 2nd ed., pp. 2002–2009. Elsevier.
Ostheim, L., Klar, P., Moryson, Y., Rohnke, M., Beyer, A., Volk, M., Munde, M., Stolz, W. & Volz, K. (2019). *J. Appl. Phys.* **126**, 215704.
Pham, H. T., Phan, C. D., Nguyen, M. T. & Tam, N. M. (2020). *RSC Adv.* **10**, 19781–19789.
Poswal, A. K., Agrawal, A., Poswal, H. K., Bhattacharyya, D., Jha, S. N. & Sahoo, N. K. (2016). *J. Synchrotron Rad.* **23**, 1518–1525.
Ravel, B. & Newville, M. (2005). *J. Synchrotron Rad.* **12**, 537–541.
Rivoire, K., Buckley, S., Hatami, F. & Vučković, J. (2011). *Appl. Phys. Lett.* **98**, 263113.
Rivoire, K., Lin, Z., Hatami, F., Masselink, W. T. & Vučković, J. (2009). *Opt. Express*, **17**, 22609–22615.
Romanato, F., De Salvador, D., Berti, M., Drigo, A., Natali, M., Tormen, M., Rossetto, G., Pascarelli, S., Boscherini, F., Lamberti, C. & Mobilio, S. (1998). *Phys. Rev. B*, **57**, 14619–14622.
Roychowdhury, R., Dixit, V. K., Vashisht, G., Sharma, T. K., Mukherjee, C., Rai, S. & Kumar, S. (2019). *Appl. Surf. Sci.* **476**, 615–622.
Roychowdhury, R., Kumar, S., Wadikar, A., Mukherjee, C., Rajiv, K., Sharma, T. K. & Dixit, V. K. (2017). *Appl. Surf. Sci.* **419**, 957–967.
Sanatinia, R., Anand, S. & Swillo, M. (2014). *Nano Lett.* **14**, 5376–5381.
Sanatinia, R., Swillo, M. & Anand, S. (2012). *Nano Lett.* **12**, 820–826.
Schliwa, A., Winkelnkemper, M., Lochmann, A., Stock, E. & Bimberg, D. (2009). *Phys. Rev. B*, **80**, 161307.
Schnohr, C., Araujo, L., Kluth, P., Sprouster, D., Foran, G. J. & Ridgway, M. C. (2008). *Phys. Rev. B*, **78**, 115201.
Shambat, G., Rivoire, K., Lu, J., Hatami, F. & Vučković, J. (2010). *Opt. Express*, **18**, 12176–12184.
Silvestri, H., Bracht, H., Hansen, J. L., Larsen, A. N. & Haller, E. (2006). *Semicond. Sci. Technol.* **21**, 758–762.
Simmonds, P. J. & Larry Lee, M. (2011). *Appl. Phys. Lett.* **99**, 123111.
Singh, R. & Bester, G. (2009). *Phys. Rev. Lett.* **103**, 063601.
Singh, S., Nand, M., Ajimsha, R., Upadhyay, A., Kamparath, R., Mukherjee, C., Misra, P., Sinha, A., Jha, S. & Ganguli, T. (2016). *Appl. Surf. Sci.* **389**, 835–839.
Supplie, O., May, M. M., Kleinschmidt, P., Nägelein, A., Paszuk, A., Brückner, S. & Hannappel, T. (2015). *APL Mater.* **3**, 126110.
Supplie, O., May, M. M., Steinbach, G., Romanyuk, O., Grosse, F., Nägelein, A., Kleinschmidt, P., Brückner, S. & Hannappel, T. (2015). *J. Phys. Chem. Lett.* **6**, 464–469.
Tormen, M., De Salvador, D., Drigo, A., Romanato, F., Boscherini, F. & Mobilio, S. (2001). *Phys. Rev. B*, **63**, 115326.
Tormen, M., De Salvador, D., Natali, M., Drigo, A., Romanato, F., Rossetto, G., Boscherini, F. & Mobilio, S. (1999). *J. Appl. Phys.* **86**, 2533–2539.
Vainshtein, B. K., Fridkin, V. M. & Indenbom, V. L. (2012). *Modern Crystallography 2 – Structure of Crystals.* Springer Science & Business Media.
Volz, K., Beyer, A., Witte, W., Ohlmann, J., Németh, I., Kunert, B. & Stolz, W. (2011). *J. Cryst. Growth*, **315**, 37–47.
Wang, W.-F., Cheng, K.-Y. & Hsieh, K.-C. (2018). *AIP Adv.* **8**, 015230.
Yarlagadda, B., Rodriguez, A., Li, P., Velampati, R., Ocampo, J., Suarez, E., Rago, P., Shah, D., Ayers, J. & Jain, F. (2008). *Appl. Phys. Lett.* **92**, 202103.
Yerino, C. D., Simmonds, P. J., Liang, B., Jung, D., Schneider, C., Unsleber, S., Vo, M., Huffaker, D. L., Höfling, S., Kamp, M. & Lee, M. L. (2014). *Appl. Phys. Lett.* **105**, 251901.